Nanoscale

ROYAL SOCIETY OF CHEMISTRY

PAPER

View Article Online
View Journal | View Issue

Cite this: *Nanoscale*, 2025, **17**, 12450

Control of Cu morphology on TaN barrier and combined Ru-TaN barrier/liner substrates for nanoscale interconnects from atomistic kinetic Monte Carlo simulations†

Samuel Aldana, * Cara-Lena Nies and Michael Nolan *

The miniaturization of electronic devices poses severe challenges for metal interconnect deposition in back-end-of-line processing due to the decreasing volume available in the interconnect via. Cu is currently used as the interconnect metal and requires barrier and liner layers to prevent diffusion into silicon and promote smooth film growth. However, these layers occupy critical space in the already narrow, high-aspect ratio interconnect vias. Designing combined barrier/liner materials is critical to optimizing available interconnect volume. While film morphology can be predicted from first principles calculations, *e.g.* Density Functional Theory (DFT), modelling deposition to understand the evolution of metal growth and optimize barrier material design and metal deposition is extremely challenging. We present an *atomistic* kinetic Monte Carlo (kMC) investigation of Cu deposition on Ru-modified TaN as a potential dual-function barrier/liner material. Using DFT-calculated activation barriers, we predict Cu morphology on these technologically important substrates at back-end-of-line processing temperatures. We evaluate 2D *vs.* 3D morphology and film quality by analyzing film roughness, island size, substrate exposure, layer occupation rate, film compactness and the effect of annealing. Our results show that Ru-modified TaN with 50% Ru incorporation significantly reduces roughness and islanding, promoting the desired 2D growth. Vacuum annealing further promotes smooth Cu films, eliminating vacancy defects on Ru-modified substrates, while TaN promotes further island formation. This demonstrates the potential of Ru-TaN in optimizing Cu deposition for advanced CMOS interconnects and showcases a new, robust approach for atomistic simulation of metal deposition on a range of substrates.

Received 29th October 2024,
Accepted 10th April 2025

DOI: 10.1039/d4nr04505j

rsc.li/nanoscale

Introduction

The continuous miniaturization of electronic devices, driven by the demand for faster but increasingly more energy-efficient technology, has been fueling the semiconductor industry. Device miniaturization enables the development of emerging data-intensive applications, such as neuromorphic computing, machine learning algorithm training, the Internet of Things (IoT) and 5G.[1] Reducing transistor channel lengths to nanometer scales not only enhances operational speed and transistor density, but also introduces performance and reliability challenges, particularly in the deposition of metal interconnects, such as Cu, in high-aspect-ratio vias. This poses a severe bottleneck for further miniaturization and critically affects the performance and reliability of nanometer-scale integrated circuits.[2–6]

Notably, the advantages of new technology nodes such as Gate All Around (GAA) and Complementary Field Effect Transistors (CFET) are negated if signal propagation delays in transistor interconnects are not correspondingly reduced. Reducing the metal cross-section in a via increases interconnect resistance, raising the resistance–capacitance (RC) time constant of the metal–dielectric interconnects, resulting in higher propagation delays.[5,7] This RC delay determines the signal propagation speed across interconnects, affecting the overall performance,[6] heat dissipation and energy consumption of integrated circuits. Further decreasing resistance and capacitance involves trade-offs, including increased complexity, higher costs, and potential impacts on device performance and reliability. This necessitates the development of new materials and processes to mitigate RC delay.[4]

Cu has been in use as the interconnect metal in integrated circuits for all technology nodes since 1997. Its low resistivity

Tyndall National Institute, University College Cork, Lee Maltings, Dyke Parade, Cork T12 R5CP, Ireland. E-mail: samuel.delgado@tyndall.ie, michael.nolan@tyndall.ie

†Electronic supplementary information (ESI) available: Estimation of activation energies, 3D layer surfaces and color maps, partial pressure comparison, RMS roughness, island sizes, substrate exposure and annealing impact on layer surfaces and roughness (PDF). See DOI: https://doi.org/10.1039/d4nr04505j

and resistance to electromigration enable faster signal transmission and improved reliability. However, as Cu interconnects are scaled down, challenges arise. Cu tends to diffuse into silicon under thermal stress, degrading its electrical properties.[3,5,8,9] To prevent this, a diffusion barrier like TaN is required.[2,6,8,10,11] Furthermore, at nanoscale dimensions, where next generation sub-nm technology nodes like GAA and CFET dominate, Cu exhibits high resistivity and forms non-conducting 3D islands, particularly during thermal treatment.[8,11] This agglomeration can cause reliability and integration issues, preventing Cu from serving as a conducting wire.[8,11] This tendency to form 3D islands rather than continuous 2D films is driven by the competition between metal–substrate and metal–metal interactions, which arises when the Cu–substrate interaction is weaker than Cu–Cu interactions, promoting upward migration of Cu atoms.[12] To mitigate this, a liner material, such as Co[13–16] and Ru,[11,16–21] can be inserted between the substrate and the adlayer to enable smooth Cu electroplating in high-aspect ratio interconnect vias.[10,17,20,22] An appropriate liner material must prevent (1) the interconnect metal agglomeration through stronger interconnect–liner adhesion than interconnect–barrier adhesion and (2) liner material agglomeration and diffusion into the interconnect through stronger adhesion of the liner to the diffusion barrier than to the interconnect metal.[22]

However, as technology miniaturizes, the available volume for the barrier/liner/interconnect stack becomes increasingly restricted, making deposition using standard methods like physical vapor deposition (PVD) more challenging.[23] Depositing two additional layers alongside the Cu interconnect in high-aspect-ratio vias can result in pinch-off or blockage.[11,19] Despite these challenges and the advances in alternative materials,[24,25] Cu remains competitive due to its stability, electrical properties,[26] and seamless integration with existing technologies.[27–29] One solution to the volume issue is designing a single material that combines barrier and liner properties for Cu deposition, such as a doped or modified metal nitride deposited using atomic layer deposition (ALD).[30] Incorporation of two metals can be achieved with ALD through laminate doping.[31,32] ALD enables conformal, thin film deposition, reduces process steps, and ensures maximum Cu content in interconnect vias.[18,21,33] Typical combined barrier/liner materials are a barrier that incorporates another metal that promotes Cu wetting, such as TaN(Ru),[11,18,19,21] Co(W),[34] 2D TaS_x [35] and amorphous $CoTi_x$.[36] This approach modulates substrate–interconnect interaction strength, controlling film growth and introducing liner properties to the barrier. Strong interactions promote 2D layer growth, while weak ones favor 3D island growth,[12,37–39] so controlling the metal–substrate interaction is key for optimizing metal deposition.

In this study, we focus on modifying TaN to deliver a combined barrier–liner material;[11] TaN is attractive due to its well-established reliability and widespread adoption in the semiconductor industry,[40–42] making it a practical and industry-compatible approach for extending Cu interconnect performance beyond current technology nodes by overcoming the challenge of Cu islanding. While Co-based alloys, such as Co(W) and amorphous $CoTi_x$, exhibit promising properties, including wetting ability and Cu diffusion coefficient, they have yet to surpass the performance of TaN in the most advanced technology nodes.[36,43] Additionally, among 2D materials—such as graphene, h-BN, MoS_2, WSe_2, and TaS_x—TaS_x has demonstrated desirable adhesion with Cu. Despite excellent scalability and diffusion barrier properties, the primary limitation of TaS_x is the high processing temperature required to achieve high-quality films, exceeding the thermal budget of back-end-of-line (BEOL) integration, posing significant challenges for industrial implementation.[44] Alternatively, atomic layer deposition (ALD)-grown MoS_2 has shown favourable diffusion barrier properties while remaining compatible with BEOL processing temperatures. However, further thickness scaling is necessary for full industrial deployment.[45] Therefore an approach to modify TaN by incorporation of another metal, Ru,[11] Co, or W,[46] shows promise for interconnects by promoting 2D deposition of copper instead of island deposition. This motivates the choice of Ru-modified TaN in the present study.

First principles Density Functional Theory (DFT) calculations have been used to investigate Cu adhesion to TaN and various liner materials,[22] the activation energy for Cu migration on doped TaN,[11,18,19] and the behavior of Cu atoms on Cu[47,48] and Ag surfaces.[49] However, DFT's high computational cost limits it to short timescales (ps) and small systems (hundreds of atoms), making it unsuitable for simulating metal deposition. Conversely, mean-field approximations offer a cost-effective alternative for larger systems over longer timescales, but lack microscopic detail.[50–52] An intermediate approach is the kinetic Monte Carlo algorithm (kMC), which captures stochastic, microscopic behavior over macroscopic timescales. kMC has proven valuable for investigating the formation and dynamics of 3D islands on weakly-interacting substrates,[12,39,53] 2D island morphology[54,55] and structural changes in devices like memristors.[56–59]

In this paper, we employ a new kMC algorithm based on DFT results to study Cu deposition on the TaN barrier with varying levels of Ru surface incorporation to yield a combined barrier/liner layer and analyze its performance in controlling Cu morphology. Previous DFT studies have investigated Cu morphology on modified TaN,[11,18,19] shedding light on early film growth stages and the role of Cu–substrate interactions, though these models are limited in scale and time. By incorporating DFT insights into the kMC simulations, we predict the quality of Cu films deposited on TaN with different Ru levels, at BEOL relevant deposition temperatures and partial pressures. We evaluate key film properties including film thickness, substrate coverage, occupation rate per layer (assessing vertical or layer-by-layer growth and substrate coverage efficiency), Root Mean Square (RMS) roughness (reflecting surface roughness), and Cu atom coordination numbers (as a measure of defect density) to evaluate the morphology. An important advance compared to the literature is our direct examination of vacuum annealing effects on Cu films, revealing how annealing promotes the desired film morphology.

Overall, this work delivers a new atomistic approach to simulate and predict metal film deposition and morphology of technologically relevant materials, essential for developing next-generation metal interconnects for GAA and CFET devices.

Results and discussion

Substrate modelling

The combined barrier/liner materials investigated are based on TaN with varying Ru concentrations in the surface layer: bare TaN, 25% Ru (Ru25) and 50% Ru (Ru50).[11] The modification involves substituting Ta sites with Ru in the top layer of TaN. This composition can be achieved through atomic layer deposition of TaN and then introducing a Ru precursor for the final cycles to incorporate Ru into the TaN surface layer. Notably, the distribution of Ru affects the electronic properties and thermal stability of the Cu structure, as the smaller ionic radius of Ru compared to Ta creates surface recesses that can trap Cu atoms, but that also decreases the thermal stability at high Ru concentrations.[11,18,19] Hence, we limited the kMC simulations to substrates with a maximum of 50% Ru incorporation because this Ru content can effectively promote 2D growth and enhance thermal stability compared to higher Ru concentrations and is feasible to fabricate using atomic layer deposition.[11] The insights obtained from DFT calculations (see the Methods section), along with previous *ab initio* studies on homoepitaxial Cu deposition,[47,48] are used in kMC simulations to investigate the deposition of Cu on the aforementioned substrates, assessing their performance as a barrier/liner material. The substrate is not explicitly included in the kMC simulations, but is instead modelled *via* the Cu migration barriers. Full details are presented in the Methods section and ESI, section 1.†

Stochastic metal deposition model

A discrete lattice kMC model was employed to simulate atom-by-atom adsorption and adatom diffusion between neighboring sites. The Cu lattice used is a (10 × 10 × 2 nm) face-centered cubic (fcc) structure with (111) orientation, Cu lattice constants $a = b = c = 0.358$ nm and periodic boundary conditions in the plane. Each Cu atom has twelve nearest neighbors, as shown in Fig. 1a. Specifically, six neighbors are in the same plane (blue particles), three are in the upper layer (orange particles) and three are in the lower layer (green particles). Fig. 1b–d present a representative simulation of a Cu film deposited on TaN at 300 K after more than 2.3 million steps giving a film thickness of 1 nm. A (111) orientation is shown in the *x*–*y* top view (Fig. 1b) and the *y*–*z* cross section

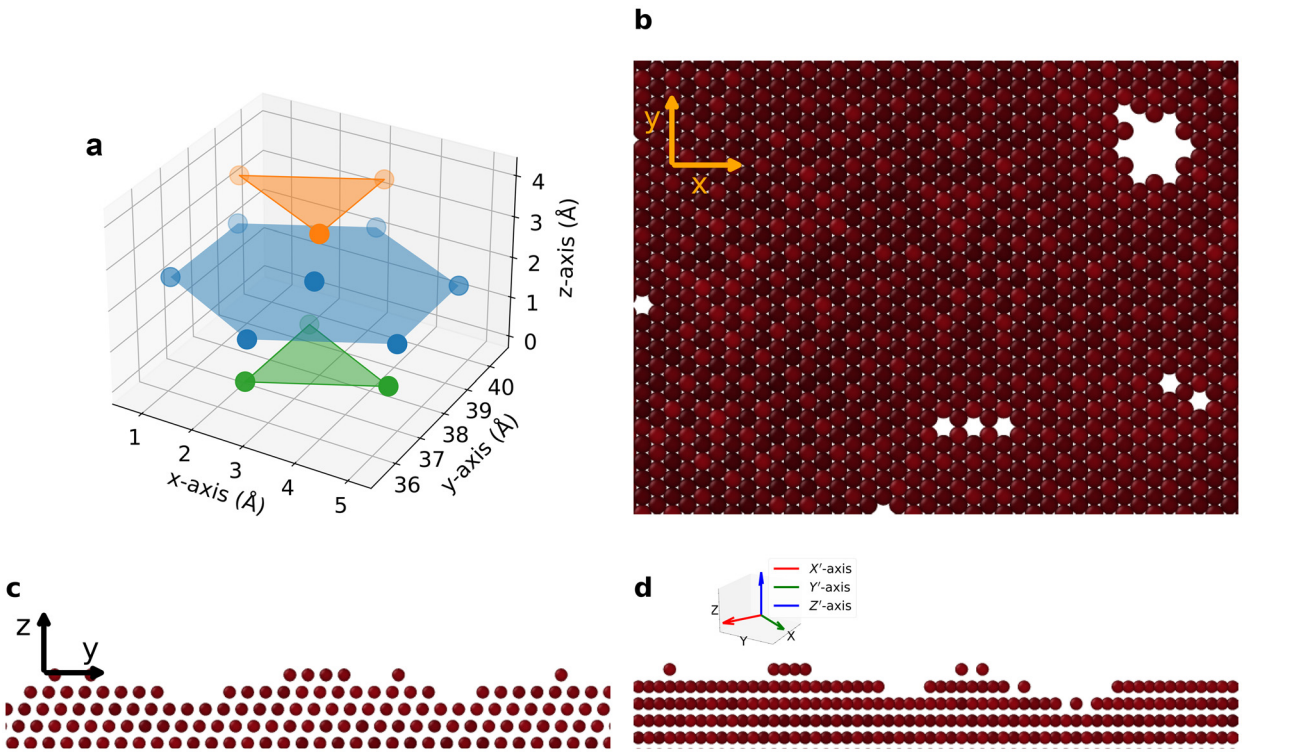

Fig. 1 (a) Atom with its twelve nearest neighbors: six neighbors are in the same plane (blue particles), three are in the upper layer (orange particles) and three are in the lower layer (green particles). A representative simulation of a Cu film deposited on a TaN substrate at 300 K after more than 2.3 million steps at a partial pressure of 0.1 Pa from different perspectives: (b) top view aligned with the *z* direction (*x*–*y* plane) displaying a (111) orientation, with atoms arranged in a close-packed hexagonal pattern. (c) Cross-section along the *x*-direction (*y*–*z* plane) displaying a (111) orientation, showing a close-packed hexagonal pattern. (d) Cross-section of the lattice in the (001) orientation, following a 30-degree rotation around the *z*-axis, exhibiting a square lattice pattern.

(Fig. 1c), while a (001) orientation is depicted in the cross-section of the lattice, rotated 30 degrees around the *z*-axis (Fig. 1d). As the film grows, it is possible to have (111) and (001)-like features appear, which have their own, distinct migration barriers for copper. The observed irregularities and gaps correspond to typical defects encountered during deposition. The main processes in the simulations are the deposition and migration of Cu atoms either on the substrate or on the growing Cu film. We implemented the following conditions for migration and adsorption processes: for migration, Cu atoms must be supported by either the substrate or at least two nearest neighbors, while for adsorption, they must have the substrate or three nearest neighbors. These conditions, free of geometric constraints, allow for the formation of various three-dimensional shapes.

Cu deposition simulation on various substrates

To investigate the impact of different substrates and deposition parameters, we modelled Cu deposition on TaN, Ru25 and Ru50 using the activation energies shown in Table 1 (Methods section) at a series of temperatures and partial pressures, keeping within the constraints of BEOL processing.

To evaluate the growth morphology and film quality we study the evolution of key metrics with time and temperature. Specifically, we examined film thickness, extent of covered substrate area and occupation rate per layer to assess the competition between vertical and layer-by-layer growth and substrate coverage efficiency. We quantify the extent of island formation and morphology through Root Mean Square (RMS) roughness, island count and the total island mass, and measure defect density by analyzing the coordination number of Cu atoms. In addition, and in contrast to typical kMC simulations of deposition processes, we explored the effects of vacuum annealing on the film properties and their influence on film morphology and quality. Higher quality films are characterized by lower substrate exposure, fewer defects and reduced RMS roughness.

Surface roughness as a measure of island formation

Fig. 2 presents the temporal evolution of key film metrics—the mean thickness, the Root Mean Square (RMS) roughness, the number of islands and the total island mass—across different substrates (TaN, Ru25 and Ru50), and temperature combinations (300 K, 500 K and 800 K) at a partial pressure of 0.5 Pa during Cu deposition simulations. Simulations were halted when the mean thickness of the deposited film reached 1 nm; above this thickness, distinctions between 2D and 3D morphology started to disappear. The resulting deposited films are depicted in Fig. S7,† with the corresponding height color maps shown in Fig. S8.† The RMS roughness provides quantitative data regarding the statistical height variations relative to the mean thickness. Islands were identified by locating the highest points in the simulation containing a Cu atom and defining clusters extending down to the mean thickness. The total island mass was calculated by summing the number of atoms within each detected island. For the analysis, only islands containing more than 10 atoms were considered. The study was extended to six different partial pressures (0.1, 0.5, 1, 10, 40 and 100 Pa), revealing that variations in pressure primarily reduce the time scale of the deposition process, while other metrics remained comparable, as illustrated in Fig. S9 (0.1, 0.5 and 1 Pa) and S10† (10, 40 and 100 Pa).

Fig. 2a shows the temporal evolution of the mean thickness. The same categories of colors are chosen for each material (purple for TaN, blue for Ru25 and brown for Ru50), with darker colors for higher temperatures. The growth rate is significantly influenced by partial pressure, which increases the flux of atoms impacting the surface. Specifically, raising the pressure from 0.1 Pa (Fig. S9a†) to 100 Pa (Fig. S10c†) reduces the time required to grow a 1 nm thick layer from 100 ms to 0.1 ms. Conversely, higher temperatures retard the deposition process. This behavior aligns with the expression for the transition rate of the deposition process (k_{ads}), derived from the kinetic gas theory and presented in the Methods section. The expression demonstrates that an increase in partial pressure raises the transition rate, while higher temperatures reduce it. The results in Fig. 2a also demonstrate that substrates with weaker interactions promote a more rapid increase in mean thickness, suggesting a preference for rapid vertical island growth over horizontal growth, driven by the lower activation energies associated with upward Cu migration. Among the substrates studied, Ru50 exhibits the slowest increase in film thickness, revealing that stronger Cu–substrate interactions prevent vertical growth and instead promote horizontal growth, which naturally yields a reduced film thickness for the same deposition time. Notably, data points for Ru50 at 300 K and TaN at 500 K exhibit significant overlap, indicating similar growth trends under these conditions.

The temporal evolution of the RMS roughness provides insights into the changes in the surface morphology of the deposited film. This analysis helps to understand the influence of the substrate interaction and growth temperature on the formation of smoother or rougher films. Generally, Cu deposited on TaN exhibits the highest RMS values, Ru25 shows intermediate values, and Ru50 presents the lowest RMS values, as shown in Fig. 2b, which is consistent with the different morphologies promoted by each substrate. For example, a Cu film deposited on a TaN substrate at 500 K and 800 K has a RMS

Table 1 Activation energies for selected Cu migration processes on Cu, TaN, Ru25 and Ru50 substrates

	Cu	TaN	Ru25	Ru50
Cu terrace (111)	0.043[47]	0.85	0.6	0.4
Cu terrace (001)	0.477[47]	—	—	—
Step ascent from substrate (111)	N/A	0.13	0.18	0.28
Step descent to substrate (111)	N/A	0.13	0.13	0.13
Step ascent from substrate (001)	N/A	0.19	0.23	0.38
Step descent to substrate (001)	N/A	0.318[48]	0.318[48]	0.318[48]
Step ascent from Cu (111)	0.313[48]	0.13	0.20	0.28
Step descent to Cu (111)	0.095[48]	0.095[48]	0.095[48]	0.095[48]
Along edge Cu (111)	0.309[48]	—	—	—
Along edge Cu (001)	0.245[48]	—	—	—

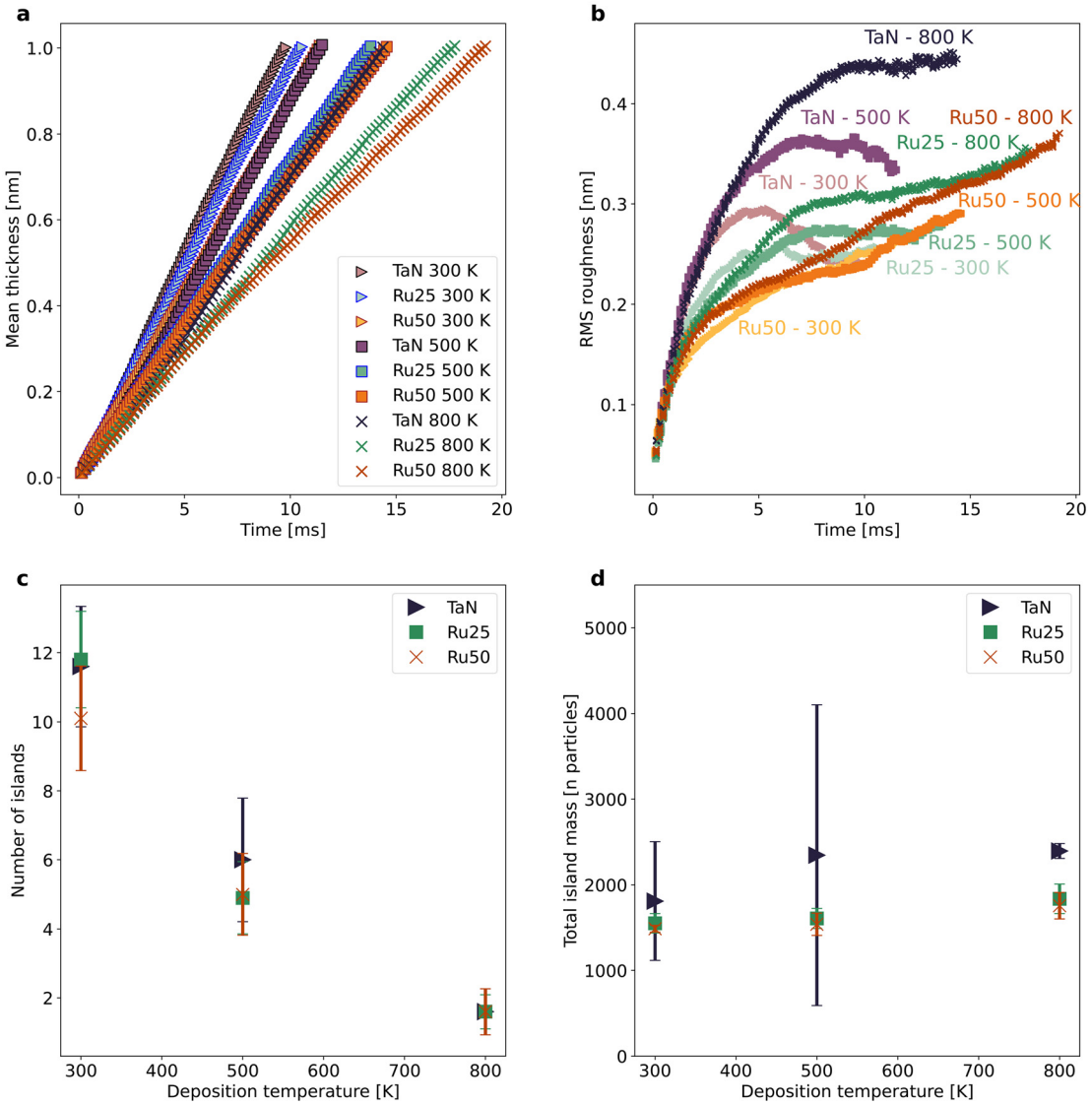

Fig. 2 Time evolution of the thickness (a), RMS roughness (b), averaged number of islands (c) and averaged total island mass (d) in deposition processes at different temperatures (300 K, 500 K and 800 K) at P = 0.5 Pa. Subfigures (a) and (b) present data from 9 independent simulations each. Subfigures (c) and (d) show the averaged results from 10 simulations per data point, with error bars as the standard deviation, totaling 90 independent simulations in each figure. Different categories of colors represent different substrates (purple for TaN, blue for Ru25 and brown for Ru50), with darker colors for higher temperatures. In (a), symbols are outlined to aid differentiation: black for TaN, blue for Ru25, and brown for Ru50.

roughness of 0.33 nm and 0.44 nm; whereas on a Ru50 substrate at the same temperatures, the RMS roughness is 12% (0.29 nm) and 16% lower (0.37 nm).

The substrate influence on the RMS roughness is further illustrated in Fig. S11† for various partial pressures with each data point being the average of 10 independent simulations. Fig. S11† also shows that elevated deposition temperatures can result in increased RMS values. This increase may be attributed to the coalescence of islands and the deepening of valleys. Specifically, Fig. S11b† shows that the film deposited on a TaN substrate at 300 K has a mean RMS roughness of 0.24 nm, while the same deposition at 800 K yields an RMS roughness of 0.44 nm. This arises from the weaker interaction of Cu and TaN, which leads to temperature-promoted island formation instead of horizontal growth.[12]

Tracking the number of islands and their total mass provides information about the growth mode and the film quality. In 2D growth, island formation is limited by the higher energy barrier for upward migration, resulting in a smaller total island mass compared with 3D growth. Consequently, the total island mass reflects Cu accumulation and surface roughness, serving as an indicator of film smoothness. Fig. 2c shows the distribution of the number of islands identified after finishing 10 deposition simulations at each temperature. The results show a decrease in the average number of islands with increasing temperature, which is attributed to the merging of islands.

While the temperature exerts a strong effect, the substrate employed plays an equally important role. Ru-modified substrates such as Ru25 and Ru50, which have stronger interactions compared to the unmodified case (TaN), generally exhibit fewer islands. Fig. S7† illustrates the surface layers and Fig. S8† the corresponding height color maps for increasing growth temperatures for the three substrates, revealing a decrease in the number of islands and an increase in their size with higher temperatures. This trend is further supported by Fig. S12,† which demonstrates that the mean island size grows with rising temperatures across a range of partial pressures (from 0.1 to 100 Pa). Fig. 2d presents the averaged total island mass from 10 deposition simulations conducted on TaN, Ru25 and Ru50 substrates at temperatures of 300 K, 500 K and 800 K. This figure quantifies the mass that migrates beyond the mean layer thickness (1 nm). Although no clear correlation with partial pressure is observed (see Fig. S9j–S9l and Fig. S10j–S10l†), the choice of substrate has a clear impact. TaN exhibits a higher total island mass compared to Ru25, while Ru50 shows the lowest values. Temperature influences Cu migration beyond the mean thickness, with TaN showing the most significant effect. Therefore, Ru incorporation improves the quality of the deposited film by hindering the upward migration of atoms, thereby reducing island formation and promoting the morphology needed for conducting Cu films.

Layer occupation as a measure of Cu morphology

The flat surface area and layer occupation analysis of deposited films offers additional information regarding the film roughness. While roughness values may be low if both islands and valleys are small, this does not guarantee the presence of large, smooth regions. Measuring the maximum flat surface area provides further quantitative analysis of a deposited film's uniformity. Additionally, the occupation rate per layer reveals how Cu is distributed across the layers, allowing for comparison with an ideally deposited film, where each layer would be fully occupied. Fig. 3 shows the evolution of the maximum flat

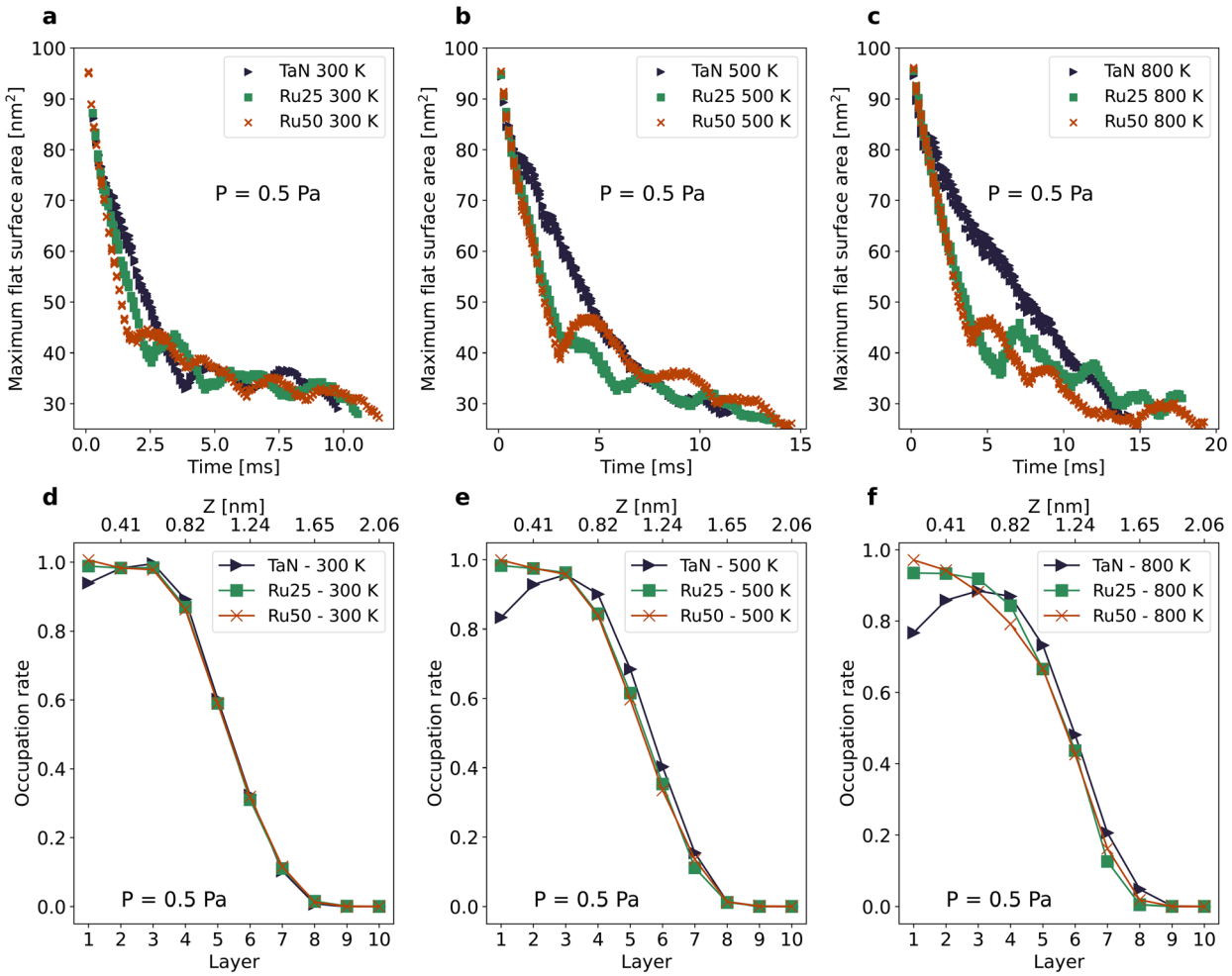

Fig. 3 Time evolution of the maximum flat surface area across all layers for Cu deposition simulations on various substrates (TaN, Ru25 and Ru50) at different temperatures: 300 K (a), 500 K (b) and 800 K (c). The occupation rate per layer at the conclusion of the simulation for the same substrates at temperatures: 300 K (d), 500 K (e) and 800 K (f). All simulations were conducted at a partial pressure of P = 0.5 Pa. The lines between points are included to guide the eyes.

surface area observed across all layers and the occupation rate per layer for Cu films deposited at P = 0.5 Pa on various substrates (TaN, Ru25 and Ru50) at different temperatures (300 K, 500 K and 800 K). The flat surface area for each layer is determined by calculating the difference between the number of occupied sites in consecutive layers $\Delta n = (n_i - n_{i+1})$, and then multiplying this difference by the area per site (0.055 nm^2).

Fig. 3a–c display how the maximum flat surface area on the surface of the layers evolves over time. Initially, the maximum flat surface area is nearly 100 nm^2, corresponding to the simulation domain, as the surface coverage is minimal with only a few scattered Cu atoms. As islands and layers grow during deposition, the flat surface area gradually decreases as these structures expand, eventually covering the underlying layer. A more rapid reduction in the flat surface area is observed for Ru25 and Ru50 compared to TaN. The observed oscillations correspond to the extension of layers (increasing values) and the coverage of underlying layers (decreasing values). The weakly interacting substrate TaN exhibits a slower reduction in the flat surface area because Cu atoms tend to form islands rather than completing layers before the deposition of the next layer starts. Higher levels of Ru concentration promote horizontal growth over vertical growth, resulting in more efficient substrate coverage and the desired 2D morphology, even at higher temperatures.

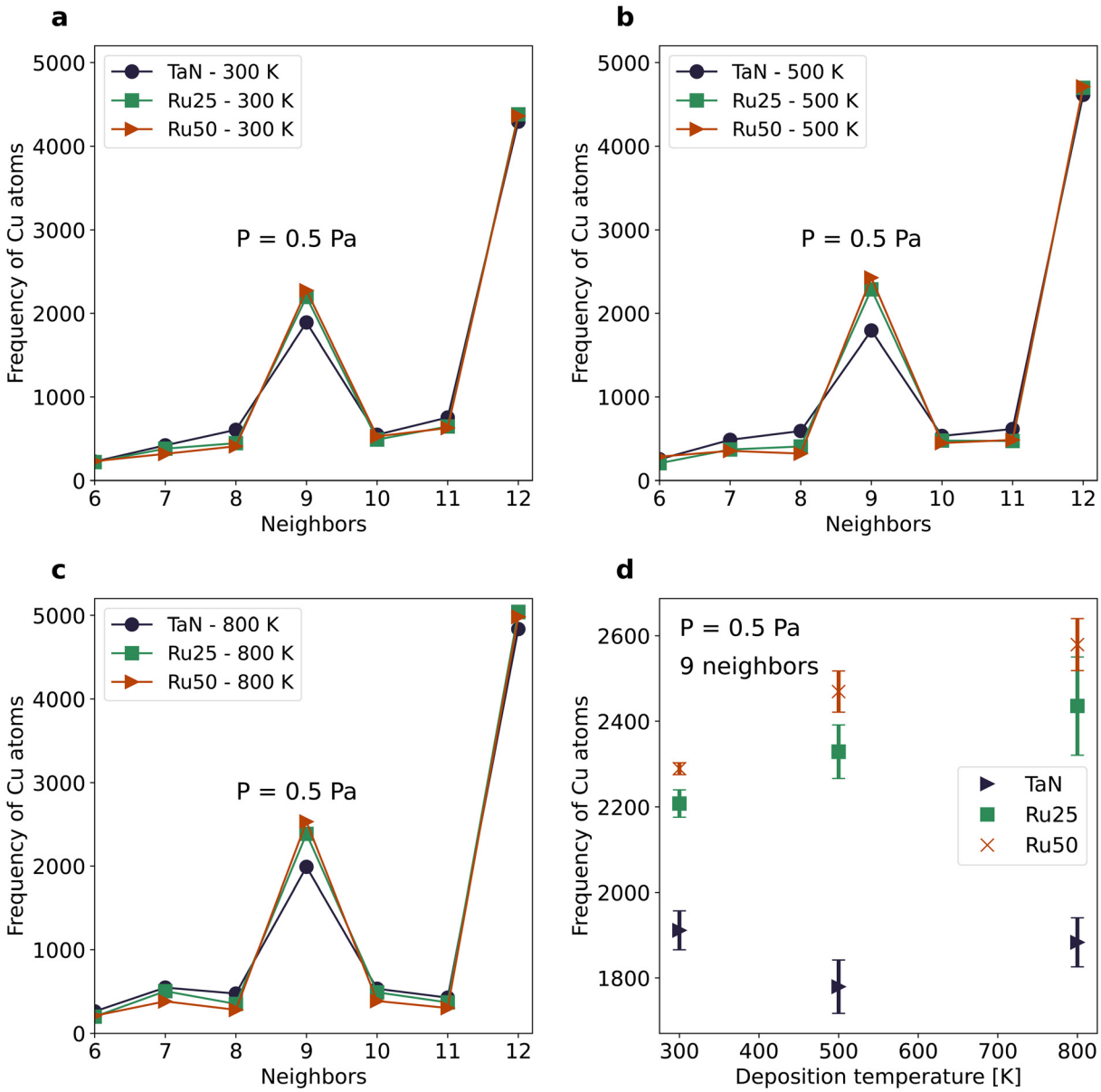

Fig. 4 Frequency distribution of Cu atoms by the number of nearest neighbors for TaN, Ru25 and Ru50 substrates at (a) 300 K, (b) 500 K and (c) 800 K. (d) Frequency of Cu atoms with 9 nearest neighbors, averaged over 10 simulations, for TaN, Ru25 and Ru50 substrates across temperatures of 300 K, 500 K and 800 K. All simulations were conducted at a partial pressure of P = 0.5 Pa.

Fig. S13a–S13c† show the substrate exposure at different temperatures, defined as the area of the substrate not covered by Cu. Averaged over 10 independent simulations, the data for partial pressures of 0.1 (Fig. S13a†), 0.5 (Fig. S13b†) and 1 Pa (Fig. S13c†) demonstrate that at 800 K, the substrate exposure for TaN (23.76 nm^2) is an order of magnitude higher compared to Ru50 (2.48 nm^2). At 500 K, TaN shows a substrate exposure of 16.46 nm^2, while Ru50 achieves complete coverage. Ru50 shows the lowest substrate exposure values, consistent with the promotion of horizontal growth and hence 2D morphology. Fig. S13d–S13f† show that elevated temperatures result in a reduction in the total flat surface area, which represents the sum of the flat surface areas across all layers. This reduction is more pronounced for the TaN substrate compared to Ru25, and is most significant when compared to Ru50. The decrease in total flat surface area occurs due to island formation, which contributes to covering the flat surfaces. This explains why Ru50 exhibits the highest flat surface area.

Fig. 3d–f display the occupation rate per layer at the end of the simulation at 300 K, 500 K, and 800 K, respectively. The data show that for TaN, the occupation rate of the first layer decreases significantly from 94% at 300 K to 77% at 800 K, suggesting that island formation becomes more favorable at higher temperatures. In contrast, the impact of temperature on Ru25 and Ru50 is less pronounced. Specifically, the occupation rate for Ru25 decreases from 99% to 93%, while for Ru50 it drops from 100% to 97%, showing that these substrates hinder island formation independently from the deposition temperature. These findings are consistent with the observations presented in Fig. S13a–S13c† regarding substrate exposure.

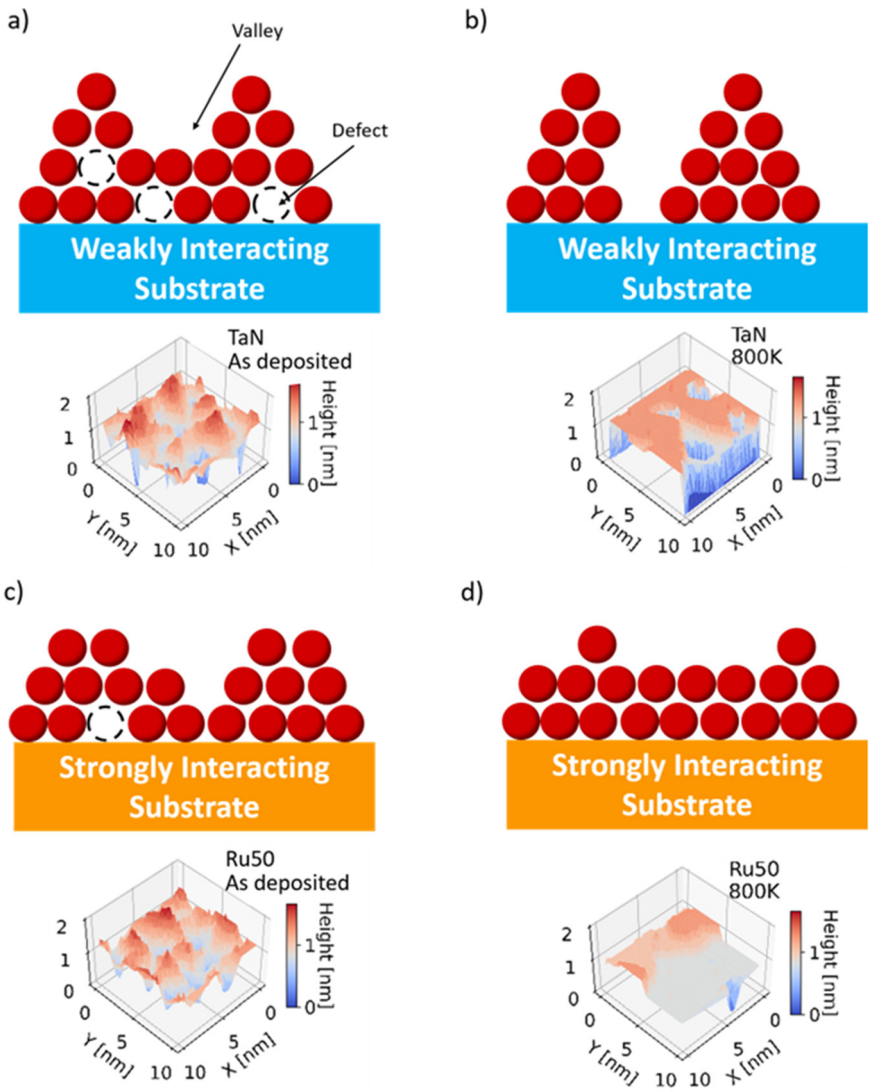

Fig. 5 Schematic and simulation of a Cu film deposited on (a) a weakly interacting substrate (TaN) before annealing, and (b) after annealing. Schematic and simulation of a Cu film deposited on (c) a strongly interacting substrate (Ru50) before annealing, and (d) after annealing. The 3D images depict the surface of the deposited Cu film, with blue indicating low regions (valleys and pits), red representing elevated regions (islands) and gray indicating flat surface area.

Defect density in deposited Cu

Analyzing the frequency of Cu atoms with a specific number of neighbors allows us to estimate the defect density within the film. In perfect bulk Cu, as shown in Fig. 1a, each Cu atom has twelve nearest neighbors: six in the same plane, three in the layer above and three in the layer below. Atoms in the top and bottom layers, however, can have a maximum of nine nearest neighbors (excluding the substrate). Thus, in an ideal crystal, all atoms would have either nine or twelve neighbors. Deviations from these coordination numbers indicate the presence of defects such as vacancies. In our case, if the first and last layers were fully occupied, we would observe 3656 Cu atoms with nine nearest neighbors. Fig. 4 presents the frequency distribution of Cu atoms based on their number of nearest neighbors, calculated after the mean layer thickness reached 1 nm for the three substrates. At all three temperatures—300 K (Fig. 4a), 500 K (Fig. 4b), and 800 K (Fig. 4c)—the number of Cu atoms with 9 neighbors is lower when Cu is deposited on TaN. In contrast, the number of atoms with fewer than 9 or 10 and 11 nearest neighbors is higher compared to the other substrates. Conversely, Ru50 shows the highest frequency of 9 nearest neighbors and the lowest frequency of cases deviating from this, that is atoms with 8, 10 or 11 nearest neighbors, while Ru25 is an intermediate case. This difference in frequency distribution for TaN and modified TaN can be explained by the stronger interaction between Cu and the Ru-modified substrates compared to bare TaN, which promotes wetting by increasing the activation energy for upward migration. As a result, Cu atoms are more likely to maximize the coordination number, promoting layer-by-layer growth rather than vertical island formation. These results suggest that Ru50 exhibits the lowest number of defects, as further evidenced in Fig. 4d and Fig. S14.† These figures show the frequency of Cu atoms with 9 and 12 nearest neighbors, averaged over 10 simulations, across a range of temperatures. Additionally, the data indicate that increasing temperature increases the number of Cu atoms with 9 (Fig. 4d) and 12 nearest neighbors (Fig. S14†), signifying a more compact layer structure. This increase is attributed to the enhanced Cu mobility at higher temperatures, which reduces the relative probability of different migrations by lowering activation energy barriers. Consequently, the temperature facilitates rearrangements of undercoordinated atoms to integrate into more stable lattice sites. This increase in the frequency of exactly 9 nearest neighbors indicates that more atoms in the bottom and top layer of the deposited Cu are fully coordinated. Along with other measures of film quality and roughness undertaken, this supports that for Ru25 and Ru50 the exposed surface area (bottom layer) and the flat surface area (top layer) increase.

Effect of vacuum annealing on film morphology and quality

Thermal vacuum annealing is a damage-healing process used in thin film deposition to reduce defects and recrystallise from an amorphous film to a crystalline film, thereby optimizing the electrical and mechanical properties of the material for

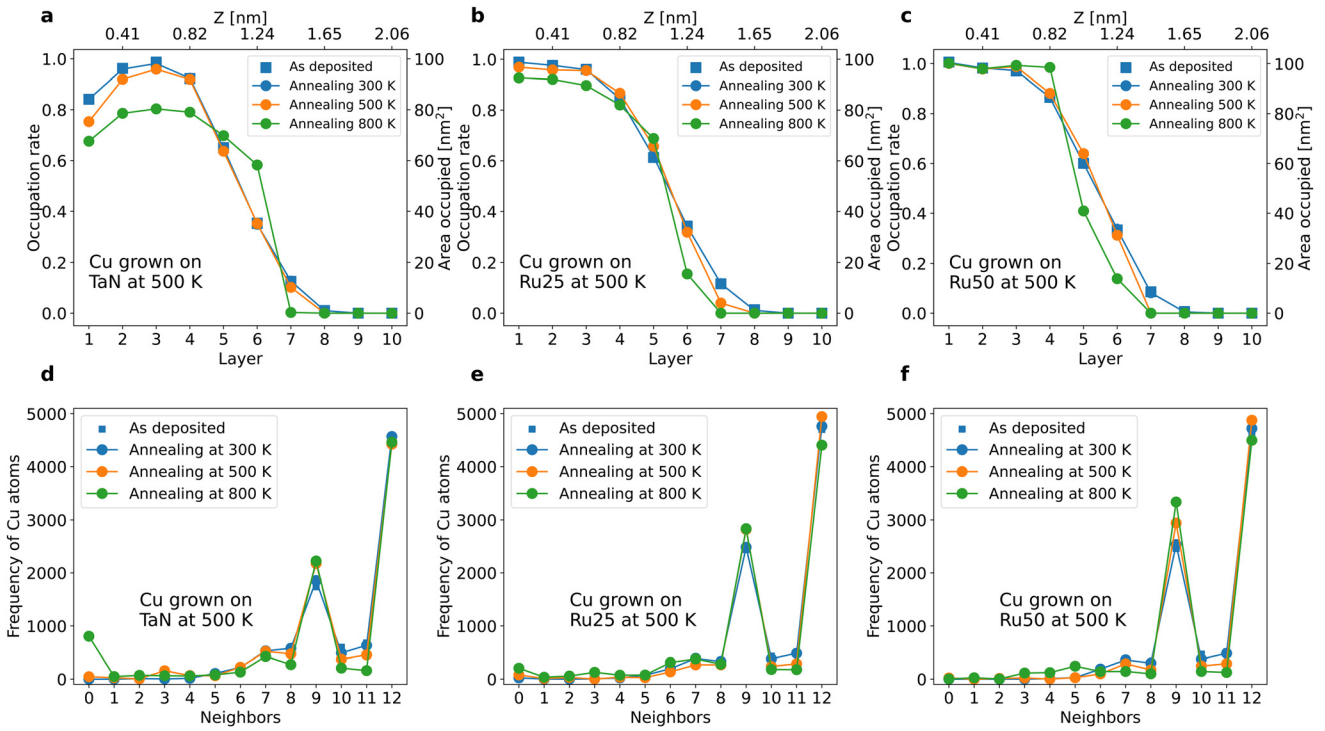

Fig. 6 The occupation rate per layer at 300 K, 500 K and 800 K annealing processes for TaN (a), Ru25 (b) and Ru50 (c). Frequency distribution of Cu atoms by the number of nearest neighbors at 300 K, 500 K and 800 K vacuum annealing for TaN (d), Ru25 (e) and Ru50 (f).

high-performance applications.[60] We explore in this section the effect of vacuum annealing on the morphology and quality of as-deposited Cu films. The temperature of annealing facilitates the migration of undercoordinated Cu atoms to more stable positions, increasing their coordination number (CN). This includes both upward migration, when not hindered by substrate interaction, and downward migration from the uppermost layers that can promote horizontal growth. For weakly interacting TaN substrates, this vacuum annealing leads to the deepening of valleys and an increase in CN for atoms within islands, as shown in Fig. 5a and b. In contrast, for strongly interacting substrates, such as Ru50, surface flattening is expected, since the high activation barriers mean that Cu atoms migrating downward rarely return to upper layers (see Fig. 5c and d). To investigate the impact on crystal quality and the potential for enhancing layer uniformity and promoting a denser atomic arrangement, Cu deposited on TaN, Ru25 and Ru50 (the same simulations discussed above) at 500 K and P = 0.5 Pa is annealed in vacuum for 2.5 million kMC steps at three temperatures: 300 K, 500 K and 800 K. We examined changes in the occupation rate (Fig. 6a–c) and the frequency distribution of Cu atoms with a specific number of nearest neighbors (Fig. 6d–f).

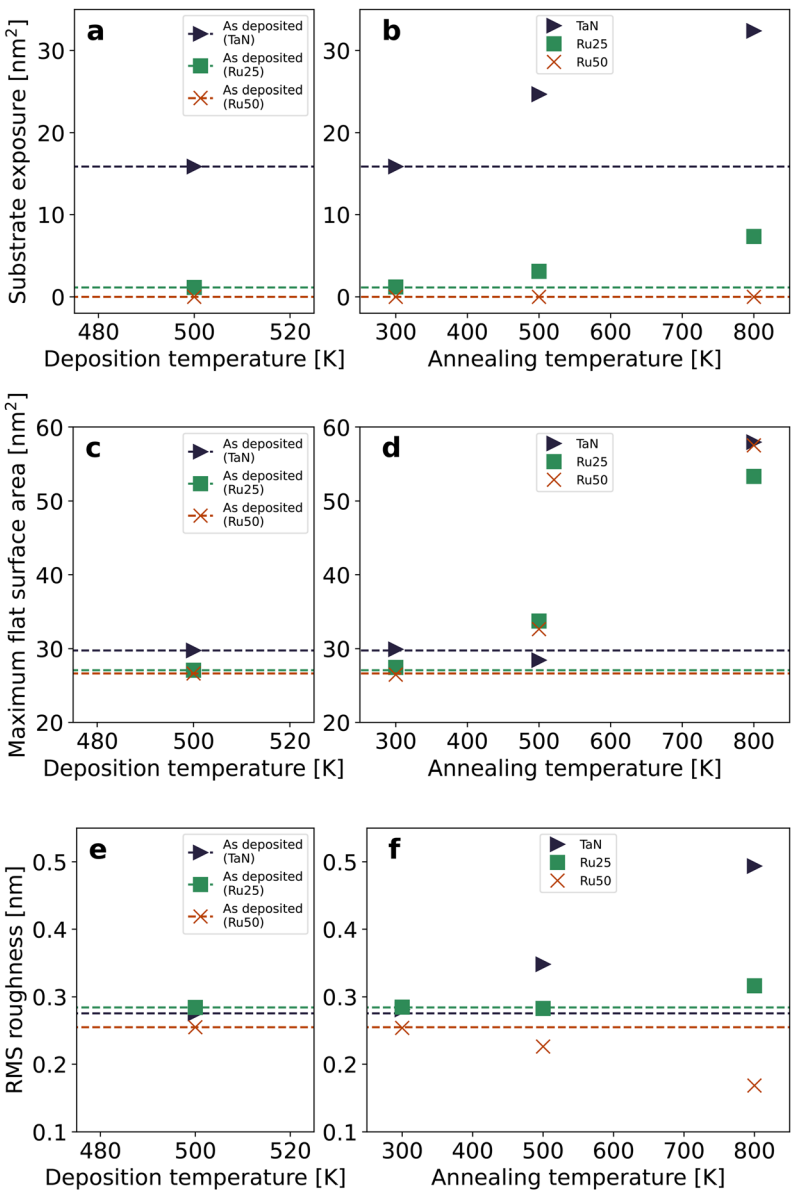

Fig. 7 Substrate exposure for as-deposited Cu at 500 K (a) and after annealing (b). Maximum flat surface area for as-deposited Cu at 500 K (c) and after annealing (d). RMS roughness for as-deposited Cu at 500 K (e) and after annealing (f). Cu is deposited at 500 K and P = 0.5 Pa on TaN, Ru25 and Ru50 and then annealed at 300 K, 500 K and 800 K. Horizontal dashed lines indicate reference values for the as-deposited films for each substrate.

Ru incorporation significantly affects the rearrangement of Cu atoms within the film at different temperatures, as illustrated in Fig. 6a (TaN), 6b (Ru25) and 6c (Ru50). Annealing at 300 K shows minimal change compared to the as-deposited films, while annealing at 500 K has a minor impact. For TaN, the occupation rate of the first layer decreases from 84% after deposition to 68% after annealing at 800 K. This indicates that annealing as-deposited Cu on TaN drives upwards Cu migration and leads to deepening of valleys (that is the space between islands is enhanced—see the surface in Fig. S15d† and the schematic in Fig. 5a and b) which increases the island uniformity. In contrast, Ru25 shows significant improvement (see Fig. S15h†), with the occupation rate of the first layer hardly decreasing, from 99% to 93%, after annealing, as shown in Fig. 6b. In this case, Fig. 6b shows how some atoms from layers below 5 also migrate upward. Conversely, for TaN, the occupation rates for layers five and six increase due to downward migration from layers above 6 and upward migration from near the substrate (Fig. 6a). Ru50 performs best, as can be seen in Fig. S15l,† maintaining a 100% occupation rate in the first layer and increased occupation rates up to the fourth layer (see Fig. 6c). This highlights the ability of Ru incorporation to minimize substrate exposure, even at high annealing temperatures, as illustrated in Fig. 7b. Notably, for Ru25 and Ru50, many atoms from layers above layer five migrate downwards, reducing both the occupation rate of layers above the sixth layer and the extent of islanding. This downward migration suggests that annealing facilitates Cu redistribution, filling layers closer to the substrate, promoting 2D growth and denser film formation, and thus enhancing crystal quality.

Cu films deposited and then annealed on Ru-TaN substrates show a reduced number of undercoordinated Cu atoms or those with no nearest neighbors compared to the TaN substrate, while increasing the frequency of atoms with 9 neighbors, particularly at higher annealing temperatures, as shown in Fig. 6d (TaN), 6e (Ru25) and 6f (Ru50). This change suggests a denser atomic arrangement, notably in the case of Ru50.

The influence of Ru incorporation into the substrate on the formation of the maximum flat surfaces during annealing is shown in Fig. 7d. While increased annealing temperature clearly promotes larger flat surface areas, the effect of the substrate is less distinct, as all substrates achieve similar surface areas. However, when examining the post-annealing surfaces of Cu deposited at 500 K on TaN, Ru25, and Ru50 (Fig. S15†), it becomes clear that Ru incorporation limits valley formation and substrate exposure (see Fig. 7b). On the TaN substrate, annealing flattens the surface, but also deepens valleys, leading to increased substrate exposure and more pronounced islands (see Fig. S15a–S15d†). A similar effect is observed for Ru25 (Fig. S15e–S15h†), where surface flattening is accompanied by reduced substrate exposure due to stronger substrate interactions. Annealing as-deposited Cu on Ru50 (Fig. S15i–S15l†), which has the strongest substrate interaction, results in the lowest substrate exposure and the smoothest surfaces, with fewer valleys. Fig. S16† provides the corresponding height color maps for the layer surfaces shown in Fig. S15.†

Analyzing RMS roughness further supports the conclusion that Ru incorporation in combination with vacuum annealing results in horizontal growth, primarily by limiting valley formation. Fig. 7f shows the RMS roughness of Cu deposited at 500 K on different substrates across the range of annealing temperatures. For TaN, annealing causes a significant increase in RMS roughness, from 0.28 nm at 300 K to 0.49 nm at 800 K. In contrast, Ru25 shows a smaller increase in RMS roughness, from 0.28 nm at 300 K to 0.32 nm at 800 K. Remarkably, for Ru50, the RMS roughness decreases with temperature, from 0.25 nm at 300 K to 0.17 nm at 800 K. Comparing the effects across substrates for Cu deposited at 300 K and 500 K (Fig. S17†) further highlights how increased Ru content improves RMS roughness, which is highly relevant for BEOL processing of Cu layers.

Conclusion

Finding combined barrier/liner materials that free up volume and promote deposition of smooth Cu interconnects while hindering island formation is key for the miniaturization of electronic devices. We have implemented a kinetic Monte Carlo simulator that uses DFT data to model Cu deposition and annealing and predict how the deposition temperature, pressure and annealing determine the morphology of deposited Cu films on TaN and Ru-modified TaN substrates. Our results demonstrate that Ru-modified TaN is a strong candidate for a combined Cu barrier and liner layer to promote improved Cu film deposition in terms of film quality and uniformity, which is crucial for the miniaturization of electronic devices to sub-nm sizes. Our kMC Cu deposition simulations on TaN substrates allow us to predict the effects of Ru incorporation in the substrate, temperature and pressure on the growth and morphology of deposited Cu. Furthermore, we study the effect of vacuum annealing on Cu morphology. This enables a new paradigm for predictive atomistic simulations of metal deposition processes on technologically important substrates, with particular target morphologies, which can be used to select suitable barrier/liner layers for controlled deposition of interconnect metal films and it can be readily extended to, *e.g.*, catalysis to predict the morphology of deposited metal nanoparticles for catalytically important reactions, thus signposting the optimal nanoparticle deposition conditions (substrate, temperature, pressure, and annealing).

Our results demonstrate that incorporating Ru into TaN substrates significantly improves their performance in promoting the deposition of conducting Cu by favoring a 2D morphology with horizontal film growth over a 3D non-conducting island morphology. At the highest level of Ru incorporation (50%) and a deposition temperature of 800 K, the surface roughness is reduced by over 16%, substrate exposure decreases by an order of magnitude and compactness is enhanced by reducing the number of undercoordinated Cu

atoms. The resulting Cu layers exhibit superior quality, even at elevated temperatures, which otherwise typically increase RMS roughness and substrate exposure during film deposition. These findings suggest that the increased substrate interaction strength from Ru incorporation promotes horizontal (2D) over vertical (3D) growth, which is crucial for achieving high-quality Cu interconnects. Vacuum annealing studies (from 300 K to 800 K) reveal that annealing at higher temperatures can further tune the morphology post deposition, depending on the substrate employed. While elevated annealing temperatures can be advantageous in reducing vacancy defects, decreasing the number of uncoordinated atoms, and promoting flatter surfaces on Ru-TaN, they can further promote Cu island formation on TaN by promoting upwards Cu migration that deepens valleys and increases substrate exposure, which in turn raises RMS roughness. This is expected given the weaker interaction between Cu and TaN as compared to Ru-TaN, which alters the growth mode to promote island formation. However, Ru incorporation mitigates these negative effects by increasing the Cu–substrate interaction and, at the highest level of incorporation (50%), can even produce beneficial effects by not only minimizing the number of uncoordinated Cu atoms but also reducing the RMS roughness. This demonstrates that Ru modification can also contribute to the stability of the layers under annealing conditions.

Methods

DFT calculations

The interaction between deposited Cu and various substrates was previously studied using periodic spin-polarized DFT with the Vienna *Ab initio* Simulation Package (VASP, version 5.4[61]).[11,18,19] The exchange–correlation functional was approximated using the Perdew–Burke–Ernzerhof (PBE) method.[62] Valence electrons were explicitly expanded in a periodic plane wave basis set with a kinetic energy cut-off of 400 eV, while core-valence electron interactions were treated using projector augmented wave (PAW) potentials.[63] The valence electron configurations used for Ta, N, Ru and Cu were Ta: $6s^2 5d^3$; N: $2s^2 2p^3$; Ru: $5s^1 4d^7$; and Cu: $4s^1 3d^{10}$.

The activation energies for Cu migration on TaN and TaN (Ru) were computed using the climbing image nudged elastic band (CI-NEB) method with 5 images including the starting and ending geometries.[64,65] The TaN supercell used for the DFT calculations has a thickness of 30.48 Å and lateral dimensions of 18.11 Å and 23.36 Å, including periodic boundary conditions and 18 Å of vacuum along the *z*-axis to prevent slab interactions along this direction. The forces acting on unconstrained atoms during geometry relaxation calculations, as well as the NEB forces in the activation energy computations, were converged to 0.02 eV $Å^{-1}$. The activation energies for Cu on crystalline Cu have been determined using molecular dynamics (MD) calculations.[47,48] Further details on the activation energies can be found in ESI, section 1.† Full details about the DFT calculations can be obtained in ref. 11.

kMC simulations

To simulate the transitions between different sites in the lattice structure and the relative likelihood of each process, we employ a rejection-free kinetic Monte Carlo algorithm. This methodology involves two steps: (1) computing the transition rates associated with each possible event and (2) using a random number to select one of these events. The transition rate of Cu migration, a thermally activated process, is determined *via* transition state theory, depending on temperature and the activation energy, *i.e.*, $\Gamma = \nu \times \exp(-E_A/E_B T)$,[66,67] where $\nu = 7 \times 10^{12}$ s^{-1} is the pre-exponential factor and E_A is the activation energy of the corresponding event. In contrast, the transition rate for the deposition process, a non-activated process, is calculated using the kinetic gas theory:[68,69] $k_{ads} = P\sigma(T,\theta)A/\sqrt{2\pi m k_B T}$, where P is the partial pressure of the gas, σ is the sticking coefficient that depends on temperature T and surface coverage θ, m = 63.546 amu is the molecular mass of Cu, A is the active area and k_B is the Boltzmann constant. The active area A is approximated by dividing the total area of the simulation domain by the number of sites. The sticking coefficient σ is set to 1, independent of T and θ, which is a commonly employed approximation.[68,69] Moreover, metals like Ag, Au, Mo, Ta and Cu typically exhibit high sticking coefficients,[70–72] often close to 1, due to the strong metallic bonding, which also promotes island formation during film growth.

The activation energies for Cu migration on various substrates, including TaN and Ru-modified TaN, have been determined using DFT calculations, with migration on TaN surfaces involving a higher activation energy compared to Ru-modified ones.[18] The migration energy barrier for the migration of Cu on the TaN substrate ranges from 0.85 to 1.26 eV.[18] In contrast, the barrier is significantly lower on bare hexagonal Ru(001), ranging from 0.07 to 0.11 eV.[18] For simplicity, we assume that the incorporation of Ru into TaN reduces the activation energy for migration on the substrate. Accordingly, we selected three values: 0.85 eV for the bare TaN, 0.6 eV for Ru25 and 0.4 eV for Ru50, which account for differences in Cu migration between the three surfaces found with DFT. As stated previously, the energy barriers for atomic Cu diffusion on an fcc metallic Cu on a (111/001) surface were previously obtained using MD.[47,48] A selection of activation energies of Cu migration processes is provided in Table 1, while further details can be found in ESI, section 1.† The activation energies for step ascent, migration from layer n to layer n + 1, on various substrates have been selected to be lower than those for homoepitaxial growth of Cu (see Table 1). This is due to the weaker interaction of TaN with Cu, compared to Cu on Cu. Meanwhile, activation energies for Cu to migrate off the substrate and form Cu islands increase with increased Ru incorporation, due to the increased interaction between Cu and Ru-TaN.[11] A bond-counting scheme is implemented to account for changes in the activation energy according to the coordination number (CN) as an atom moves from the initial to the final site. The contribution of the CN to the activation energy is 0.15 eV per atom. Typically, the migration of Cu atoms on a Cu (111) surface maintains the

same CN number with 3 neighboring Cu atoms. However, when Cu migrates upward to the next layer (step ascent on the Cu film deposited on a TaN substrate), the CN changes from 5 neighboring Cu atoms (three in the lower layer and two in the same layer) to only 2 Cu atoms supporting the migration. This transition then results in an activation energy of 0.58 eV, due to the CN change. The substrate is not explicitly included in the simulation; instead, its influence is incorporated through the activation energy sets specifically calculated for the three different substrates, thereby capturing its influence on Cu deposition. Directly modelling the influence of the substrate on Cu growth requires more advanced methodologies, such as adaptive kMC[73] approaches, *e.g.* off-lattice kMC. These techniques enable on-the-fly calculations of migration pathways and activation energy variations, allowing for a more precise description of atomic-scale interactions and dynamic surface evolution, although they significantly increase the computational overhead.

The DFT simulations for these substrates showed no migration or exchange of substrate and Cu species after depositing Cu, so no migration of Ta, N or Ru out of the substrate or Cu into the substrate is allowed in the kMC simulation.

We employ a binary tree data structure to sort the transition rates, facilitating the use of a binary search method for efficiently identifying a chosen event.[74,75] The time step is calculated with a second random number and is weighted by the transition rates: $t = -\ln(\text{rand})/\sum \Gamma$, where rand is a random number between 0 and 1 and $\sum \Gamma$ is the summation of the possible events.

Author contributions

S. A. developed and conducted the kMC simulations. C-L. N. conducted the DFT simulations. S. A., C-L. N. and M. N. analyzed the data. M. N. supervised the project. The manuscript was written through contributions of all authors. All authors have given approval to the final version of the manuscript.

Data availability

The code for the kMC simulator can be found at **https://github.com/aldanads/Material-deposition-interconnects**. The version of the code employed for this study corresponds to the "main" branch, commit on July 10, 2024 (1a4689f).

Conflicts of interest

There are no conflicts of interest to declare.

Acknowledgements

M. N. and S. A. received support from the ASCENT + Access to the European Infrastructure Nanoelectronics Program, funded through the EU Horizon Europe Programme, grant no 871130. C-L. N. and M. N. were supported through the Science Foundation Ireland SFI–NSF China Partnership Program, grant number 17/NSFC/5279.

References

1 IEEE International Roadmap for Devices and Systems, *Institute of Electrical and Electronics Engineers*, 2023, preprint. DOI: 10.60627/0P45-ZJ55.
2 N. Srivastava and K. Banerjee, *JOM*, 2004, **56**, 30–31.
3 B. Li, C. Christiansen, D. Badami and C.-C. Yang, *Microelectron. Reliab.*, 2014, **54**, 712–724.
4 M. H. Lee and W. S. Shue, in 2020 IEEE International Electron Devices Meeting (IEDM), IEEE, San Francisco, CA, USA, 2020, pp. 32.1.1–32.1.4.
5 P. S. Peercy, *Nature*, 2000, **406**, 1023–1026.
6 A. Chaudhry, *J. Semicond.*, 2013, **34**, 066001.
7 A. Ceyhan, *IEEE Trans. Electron Devices*, 2013, **60**, 4041.
8 Y.-L. Cheng, T.-J. Chiu, B.-J. Wei, H.-J. Wang, J. Wu and Y.-L. Wang, *J. Vac. Sci. Technol., B: Nanotechnol. Microelectron.: Mater., Process., Meas., Phenom.*, 2010, **28**, 567–572.
9 C.-K. Hu and B. Luther, *Mater. Chem. Phys.*, 1995, **41**, 1–7.
10 C. Zhao, Z. Tőkei, A. Haider and S. Demuynck, *Microelectron. Eng.*, 2007, **84**, 2669–2674.
11 C.-L. Nies, S. K. Natarajan and M. Nolan, *Chem. Sci.*, 2022, **13**, 713–725.
12 V. Gervilla, G. A. Almyras, F. Thunström, J. E. Greene and K. Sarakinos, *Appl. Surf. Sci.*, 2019, **488**, 383–390.
13 M. He, X. Zhang, T. Nogami, X. Lin, J. Kelly, H. Kim, T. Spooner, D. Edelstein and L. Zhao, *J. Electrochem. Soc.*, 2013, **160**, D3040–D3044.
14 Z. Li, R. G. Gordon, D. B. Farmer, Y. Lin and J. Vlassak, *Electrochem. Solid-State Lett.*, 2005, **8**, G182.
15 X. Zhang, L. Cao, V. Ryan, P. S. Ho, B. Taylor, C. Witt and C. Labelle, *ECS J. Solid State Sci. Technol.*, 2015, **4**, N3177–N3179.
16 K.-T. Jang, S.-Y. Lee, S.-K. Na, S.-K. Lee, J.-M. Baek, W.-K. You, O.-H. Park, R.-H. Kim, H.-S. Oh and Y.-C. Joo, *IEEE Electron Device Lett.*, 2018, **39**, 1050–1053.
17 X.-P. Qu, J.-J. Tan, M. Zhou, T. Chen, Q. Xie, G.-P. Ru and B.-Z. Li, *Appl. Phys. Lett.*, 2006, **88**, 151912.
18 S. Kondati Natarajan, C.-L. Nies and M. Nolan, *J. Mater. Chem. C*, 2019, **7**, 7959–7973.
19 S. Kondati Natarajan, C.-L. Nies and M. Nolan, *J. Chem. Phys.*, 2020, **152**, 144701.
20 H. Kim, Y. Naito, T. Koseki, T. Ohba, T. Ohta, Y. Kojima, H. Sato and Y. Shimogaki, *Jpn. J. Appl. Phys.*, 2006, **45**, 2497.
21 C.-C. Yang, S. Cohen, T. Shaw, P.-C. Wang, T. Nogami and D. Edelstein, *IEEE Electron Device Lett.*, 2010, **31**, 722–724.
22 B. Han, J. Wu, C. Zhou, B. Chen, R. Gordon, X. Lei, D. A. Roberts and H. Cheng, *Angew. Chem., Int. Ed.*, 2010, **49**, 148–152.

23 Z. Wu, R. Li, X. Xie, W. Suen, J. Tseng, N. Bekiaris, R. Vinnakota, K. Kashefizadeh and M. Naik, in *2018 IEEE International Interconnect Technology Conference (IITC)*, IEEE, Santa Clara, CA, USA, 2018, pp. 149–151.
24 C.-L. Lo, 2020, 4486468 Bytes.
25 H. J. Han, S. Kumar, G. Jin, X. Ji, J. L. Hart, D. J. Hynek, Q. P. Sam, V. Hasse, C. Felser, D. G. Cahill, R. Sundararaman and J. J. Cha, *Adv. Mater.*, 2023, **35**, 2208965.
26 W.-H. Xu, L. Wang, Z. Guo, X. Chen, J. Liu and X.-J. Huang, *ACS Nano*, 2015, **9**, 241–250.
27 T. Osaka and M. Yoshino, in *Electrochemical Nanotechnologies*, ed. T. Osaka, M. Datta and Y. Shacham-Diamand, Springer New York, New York, NY, 2010, pp. 255–274.
28 J. P. Gambino, in Proceedings of 2011 International Symposium on VLSI Technology, Systems and Applications, 2011, pp. 1–2.
29 D. C. Edelstein, in 2017 IEEE International Electron Devices Meeting (IEDM), IEEE, San Francisco, CA, USA, 2017, pp. 14.1.1–14.1.4.
30 S. M. George, *Chem. Rev.*, 2010, **110**, 111–131.
31 A. Paskaleva, K. Buchkov, A. Galluzzi, D. Spassov, B. Blagoev, T. Ivanov, V. Mehandzhiev, I. A. Avramova, P. Terzyiska, P. Tzvetkov, D. Kovacheva and M. Polichetti, *ACS Omega*, 2022, **7**, 43306–43315.
32 B. Blagoev, P. Terziyska, V. Mehandzhiev, P. Tzvetkov, D. Kovacheva, I. Avramova, T. Ivanova, K. Gesheva and A. Paskaleva, *J. Phys.: Conf. Ser.*, 2020, **1492**, 012053.
33 D. V. Greenslit and E. Eisenbraun, *ECS Trans.*, 2011, **35**, 17–24.
34 H. Shimizu, K. Sakoda, T. Momose and Y. Shimogaki, *Jpn. J. Appl. Phys.*, 2014, **53**, 089202.
35 C. Lo, M. Catalano, A. Khosravi, W. Ge, Y. Ji, D. Y. Zemlyanov, L. Wang, R. Addou, Y. Liu, R. M. Wallace, M. J. Kim and Z. Chen, *Adv. Mater.*, 2019, **31**, 1902397.
36 M. Hosseini, *J. Alloys Compd.*, 2017, **721**, 134–142.
37 A. Jamnig, D. G. Sangiovanni, G. Abadias and K. Sarakinos, *Sci. Rep.*, 2019, **9**, 6640.
38 A. Jamnig, N. Pliatsikas, M. Konpan, J. Lu, T. Kehagias, A. N. Kotanidis, N. Kalfagiannis, D. V. Bellas, E. Lidorikis, J. Kovac, G. Abadias, I. Petrov, J. E. Greene and K. Sarakinos, *ACS Appl. Nano Mater.*, 2020, **3**, 4728–4738.
39 B. Lü, G. A. Almyras, V. Gervilla, J. E. Greene and K. Sarakinos, *Phys. Rev. Mater.*, 2018, **2**, 063401.
40 K.-H. Min, K.-C. Chun and K.-B. Kim, *J. Vac. Sci. Technol., B: Microelectron. Nanometer Struct. – Process., Meas., Phenom.*, 1996, **14**, 3263–3269.
41 D. Edelstein, C. Uzoh, C. Cabral, P. DeHaven, P. Buchwalter, A. Simon, E. Cooney, S. Malhotra, D. Klaus, H. Rathore, B. Agarwala and D. Nguyen, in *Proceedings of the IEEE* 2001 *International Interconnect Technology Conference (Cat. No.01EX461)*, 2001, pp. 9–11.
42 C.-C. Yang, T. Shaw, A. Simon and D. Edelstein, *Electrochem. Solid-State Lett.*, 2010, **13**, H197.
43 Y.-H. Su, J.-N. Shih, Y.-S. Wang, W.-H. Tseng, W.-H. Liao, C.-Y. Hung, W.-H. Lee and Y.-L. Wang, in *2015 International Symposium on Next-Generation Electronics (ISNE)*, 2015, pp. 1–3.
44 C.-L. Lo, B. A. Helfrecht, Y. He, D. M. Guzman, N. Onofrio, S. Zhang, D. Weinstein, A. Strachan and Z. Chen, *J. Appl. Phys.*, 2020, **128**, 080903.
45 J. (Sanne) H. Deijkers, A. A. de Jong, M. J. Mattinen, J. J. P. M. Schulpen, M. A. Verheijen, H. Sprey, J. W. Maes, W. (Erwin) M. M. Kessels, A. A. Bol and A. J. M. Mackus, *Adv. Mater. Interfaces*, 2023, **10**, 2202426.
46 C.-L. Nies and M. Nolan, *J. Phys. Mater.*, 2023, **6**, 035008.
47 S. Y. Kim, I.-H. Lee and S. Jun, *Phys. Rev. B:Condens. Matter Mater. Phys.*, 2007, **76**, 245407.
48 S. Y. Kim, I.-H. Lee and S. Jun, *Phys. Rev. B:Condens. Matter Mater. Phys.*, 2007, **76**, 245408.
49 S. S. Hayat, M. Alcántara Ortigoza, M. A. Choudhry and T. S. Rahman, *Phys. Rev. B:Condens. Matter Mater. Phys.*, 2010, **82**, 085405.
50 J. Soethoudt, F. Grillo, E. A. Marques, J. R. van Ommen, Y. Tomczak, L. Nyns, S. Van Elshocht and A. Delabie, *Adv. Mater. Interfaces*, 2018, **5**, 1800870.
51 F. Grillo, H. Van Bui, J. A. Moulijn, M. T. Kreutzer and J. R. van Ommen, *J. Phys. Chem. Lett.*, 2017, **8**, 975–983.
52 F. Grillo, J. A. Moulijn, M. T. Kreutzer and J. R. Van Ommen, *Catal. Today*, 2018, **316**, 51–61.
53 V. Gervilla, G. A. Almyras, B. Lü and K. Sarakinos, *Sci. Rep.*, 2020, **10**, 2031.
54 G. S. Sun and H. Jónsson, *J. Electrochem. Soc.*, 2022, **169**, 102503.
55 S. Aldana, L. Wang, I. A. Spiridon and H. Zhang, *Adv. Mater. Interfaces*, 2024, 2400209.
56 S. Aldana, J. Jadwiszczak and H. Zhang, *Nanoscale*, 2023, **15**, 6408–6416.
57 S. Aldana, P. García-Fernández, A. Rodríguez-Fernández, R. Romero-Zaliz, M. B. González, F. Jiménez-Molinos, F. Campabadal, F. Gómez-Campos and J. B. Roldán, *J. Phys. D: Appl. Phys.*, 2017, **50**, 335103.
58 S. Aldana, P. Garciá-Fernández, R. Romero-Zaliz, M. B. González, F. Jiménez-Molinos, F. Gómez-Campos, F. Campabadal and J. B. Roldán, *J. Phys. D: Appl. Phys.*, 2020, **53**, 225106.
59 S. Aldana, J. B. Roldán, P. García-Fernández, J. Suñe, R. Romero-Zaliz, F. Jiménez-Molinos, S. Long, F. Gómez-Campos and M. Liu, *J. Appl. Phys.*, 2018, **123**, 154501.
60 U. Lafont, H. V. Zeijl and S. V. D. Zwaag, *Microelectron. Reliab.*, 2012, **52**, 71–89.
61 G. Kresse and J. Furthmüller, *Phys. Rev. B:Condens. Matter Mater. Phys.*, 1996, **54**, 11169–11186.
62 J. P. Perdew, K. Burke and M. Ernzerhof, *Phys. Rev. Lett.*, 1996, **77**, 3865–3868.
63 G. Kresse and D. Joubert, *Phys. Rev. B:Condens. Matter Mater. Phys.*, 1999, **59**, 1758–1775.
64 G. Henkelman and H. Jónsson, *J. Chem. Phys.*, 2000, **113**, 9978–9985.
65 G. Henkelman, B. P. Uberuaga and H. Jónsson, *J. Chem. Phys.*, 2000, **113**, 9901–9904.
66 C. C. Battaile, *Comput. Methods Appl. Mech. Eng.*, 2008, **197**, 3386–3398.

67 N. Cheimarios, D. To, G. Kokkoris, G. Memos and A. G. Boudouvis, *Front. Phys.*, 2021, **9**, 631918.
68 S. Kim, H. An, S. Oh, J. Jung, B. Kim, S. K. Nam and S. Han, *Comput. Mater. Sci.*, 2022, **213**, 111620.
69 M. Shirazi and S. D. Elliott, *J. Comput. Chem.*, 2014, **35**, 244–259.
70 C. F. Abrams and D. B. Graves, *J. Appl. Phys.*, 1999, **86**, 2263–2267.
71 L. Bachmann and J. J. Shin, *J. Appl. Phys.*, 1966, **37**, 242–246.
72 W. Bennett, J. Leavitt and C. Falco, *Phys. Rev. B:Condens. Matter Mater. Phys.*, 1987, **35**, 4199–4204.
73 L. Xu and G. Henkelman, *J. Chem. Phys.*, 2008, **129**, 114104.
74 A. F. Voter, Introduction to the kinetic Monte Carlo method, in *Radiation Effects in Solids*, ed. K. E. Sickafus, E. A. Kotomin and B. P. Uberuaga, Springer Netherlands, Dordrecht, 2007, pp. 1–23.
75 A. Chatterjee and D. G. Vlachos, *J. Comput.-Aided Mater. Des.*, 2007, **14**, 253–308.